Laser transverse modes of spherical resonators: a review [Invited]

Y. F. Chen*, C. C. Lee, C. H. Wang, and M. X. Hsieh

Department of Electrophysics, Taiwan Chiao Tung University, Hsinchu 30010
**Corresponding author: yfchen@cc.nctu.edu.tw*

Received May 8, 2020; accepted May 27, 2020; posted online July 24, 2020

The study of structured laser beams has been one of the most active fields of research for decades, particularly in exploring laser beams with orbital angular momentum. The direct generation of structured beams from laser resonators is deeply associated with the formation of transverse modes. The wave representations of transverse modes of spherical cavities are usually categorized into Hermite–Gaussian (HG) and Laguerre–Gaussian (LG) modes for a long time. Enormous experimental results have revealed that the generalized representation for the transverse modes is the Hermite–LG (HLG) modes. We make a detailed overview for the theoretical description of the HLG modes from the representation of the spectral unitary group of order 2 in the Jordan–Schwinger map. Furthermore, we overview how to derive the integral formula for the elliptical modes based on the Gaussian wave-packet state and the inverse Fourier transform. The relationship between the HLG modes and elliptical modes is linked by the quantum Fourier transform. The most striking result is that the HLG modes can be exactly derived as the superposition of the elliptical modes without involving Hermite and Laguerre polynomials. Finally, we discuss the application of the HLG modes in characterizing the propagation evolution of the vortex structures of HG beams transformed by an astigmatic mode converter. This overview certainly provides not only a novel formula for transverse modes, but also a pedagogical insight into quantum physics.

Keywords: transverse mode; spherical cavity; Hermite–Gaussian mode; Laguerre–Gaussian mode.
doi: 10.3788/COL202018.091404.

The quantum harmonic oscillator is an indispensable paradigm to understand the concept of quantum-classical correspondence, quantized radiation fields, and quantum optics. The eigenmodes of the two-dimensional (2D) quantum harmonic oscillator can be analytically solved as Hermite–Gaussian (HG) modes with rectangular symmetry or Laguerre–Gaussian (LG) modes with circular symmetry[1]. Since the paraxial wave equation for the spherical laser cavity is identical to the Schrödinger equation for the 2D harmonic oscillator, the HG and LG eigenmodes play an important role in exploring the laser transverse modes[2–4]. With the advent of end-pumped configurations, the high-order HG modes[5–8] and LG modes[9–15] can be efficiently generated in diode-pumped solid-state lasers. The Ince–Gaussian (IG) modes, another form of eigenfunctions to the paraxial wave equation, have been recently introduced[16] and been also experimentally observed in stable resonators[17–19].

The study of optical pattern formation has been one of the most active fields of research for decades[20–25]. Based on Hamilton's optico-mechanical theory[26,27], modern laser resonators have been widely used to analogously explore the formation of quantum coherent waves in the mesoscopic regime[28–41]. There are some intriguing features in the spatial structures of high-order transverse modes, such as low divergence of Bessel beams[42], orbital angular momentum (OAM) of helical beams[43], free acceleration of Airy beams[44], and evolution of light pulse in a nonlinear laser cavity[45]. Moreover, several interesting issues for generating optical vortices have been explored, such as the formation of vortex lattices in transverse-mode-locked processing[46,47], the phenomenon of Berezinskii–Kosterlitz–Thouless phase transition[48–50], and twisted speckle patterns[51].

The general forms characterizing scalar monochromatic optical waves are complex-valued functions that can be expressed as the real and imaginary parts. Intersections of nodal lines of real and imaginary parts are isolated zeros, so-called phase singularities[52]. Since singular points are surrounded by a circulating phase, they are typically related to the formation of optical vortices[53]. Consequently, the terms phase singularity and optical vortex are often used interchangeably. Optical vortex beams[54,55] carrying OAM can be used in various fields[56], including optical tweezers[57–60], trapping and guiding of cold atoms[61–63], radio communications[64,65], and quantum information processing[66]. Several techniques have been presented to create optical vortex beams[67,68]. Abramochkin and Volostnikov originally used an astigmatic mode converter (AMC) formed by a matched pair of cylindrical lenses to generate the so-called Hermite–LG (HLG) beams[69]. The HLG beams, a continuous evolution between HG and LG beams, can successively be realized by rotating the cylindrical lens about the optical axis by an angle ζ.

Ellipses are the classical periodic orbits in the 2D isotropic harmonic oscillator. Pollet *et al.*[70] theoretically exploited the special unitary group of degree 2 [SU(2)] coherent state to demonstrate the quantum wave functions localized on elliptical orbits. It has been universally found that quantum wave functions localized on classical periodic orbits are associated with striking quantum

phenomena such as conductance fluctuations in mesoscopic semiconductor billiards[71,72], oscillations in photodetachment cross sections[73,74], and shell effects in metallic clusters[75,76]. In laser physics, we have experimentally used a diode-pumped solid-state laser to observe the elliptical modes corresponding to the SU(2) coherent state[77,78]. Mathematically, the SU(2) elliptical mode is a superposition of the degenerate HG modes[79]. We have recently verified that elliptical modes and HG modes can form a quantum Fourier transform pair[80]. From the representation of the quantum coherent state, we have inventively derived the elliptical mode to be as an integration of the 2D Gaussian wave packet over the elliptical orbit without involving the HG modes. The derived integral formula can be extensively employed to compute not only elliptical modes but also HLG modes in a supereefficient way.

In this article, we exploit the Schwinger's SU(2) transformation[81] to systematically overview the wave representation of the HLG transverse modes of spherical laser resonators. The SU(2) representation for the HLG modes analytically connects the HG and LG modes through the rotational transformation on the Poincaré sphere. On the other topic, we review the wave representation of the elliptical modes by extending the one-dimensional (1D) Schrödinger coherent state to the 2D coherent state. The integral formula of the elliptical modes is comprehensively derived as the integration of the Gaussian wave packet over the elliptical trajectory. We further exploit the quantum Fourier transform to decompose the HG mode as a coherent superposition of elliptical modes corresponding to a bundle of elliptical orbits. We also overview that the decomposition of the HG mode can be extended to express the HLG mode as a coherent superposition of elliptical modes corresponding to a bundle of elliptical orbits under the SU(2) transformation. The overwhelming superiority of representing the HLG modes based on the elliptical modes is the direct manifestation of the wave-ray (quantum-classical) connection without involving the special functions of Hermite and Laguerre polynomials. Finally, we overview how to employ the wave representation of the HLG modes to characterize the propagation evolution of the vortex structures of HG beams transformed by a single lens AMC with arbitrary angle ζ. Since laser modes with OAM have been intensively studied over the past few years[82–86], the present analysis certainly provides not only a pedagogical insight into quantum physics but also a novel formula for generating optical vortices.

The transverse modes in the spherical cavity are identical to the eigenfunctions in the 2D isotropic harmonic oscillator. In terms of the ladder operators, the Hamiltonian of the 2D isotropic oscillator is given by[87]

$$H_o = (a_1^\dagger a_1 + a_2^\dagger a_2 + 1)\hbar\omega_o, \tag{1}$$

where $a_1 = (x + ip_x)$, $a_1^\dagger = (x - ip_x)$, $a_2 = (y + ip_y)$, and $a_2^\dagger = (y - ip_y)$ are ladder operators in the quantum harmonic oscillator, $\hbar$ is the reduced Planck constant, and ω_o is the natural frequency. The eigenfunctions of H_o are given by[2–4]

$$\psi_{n_1,n_2}^{(\mathrm{HG})}(\tilde{x},\tilde{y}) = (2^{n_1+n_2} n_1!\, n_2!\, \pi)^{-1/2}\, e^{-(\tilde{x}^2+\tilde{y}^2)/2} H_{n_1}(\tilde{x}) H_{n_2}(\tilde{y}), \tag{2}$$

where n_1 and n_2 are the quantum numbers, $\tilde{x} = x\sqrt{\mu\omega_o/\hbar}$ and $\tilde{y} = y\sqrt{\mu\omega_o/\hbar}$ are the dimensionless variables for the xy space, μ is the oscillator mass, and $H_n(\cdot)$ is the Hermite polynomials of order n. In laser physics, the eigenfunctions in Eq. (2) are usually called the HG modes. Due to the symmetry of rotational invariance, the representation of the eigenfunctions of H_o can be generalized by performing the SU(2) transformation of HG modes.

Schwinger utilized the Jordan map to work out the theory of quantum angular momentum and proposed the J_i operators as[81,87–89]

$$J_1 = (a_1^\dagger a_2 + a_2^\dagger a_1)/2, \tag{3}$$

$$J_2 = -i(a_1^\dagger a_2 - a_2^\dagger a_1)/2, \tag{4}$$

$$J_3 = (a_1^\dagger a_1 - a_2^\dagger a_2)/2. \tag{5}$$

The J_i operators satisfy the usual angular-momentum commutation relations, i.e., Lie commutator algebra $[J_i, J_j] = i\varepsilon_{i,j,k} J_k$, where the Levi–Civita tensor $\varepsilon_{i,j,k}$ is equal to $+1$ and -1 for even and odd permutations of its indices, respectively, and zero otherwise. Note that the J_i operators can be expressed as the image of the Pauli matrices $\boldsymbol{\sigma}$ of SU(2) in the Jordan map: $\mathbf{J} = \mathbf{a}^\dagger(\boldsymbol{\sigma}/2)\mathbf{a}$. It is known from classical mechanics that an arbitrary rotation of a rigid body can be expressed in terms of the Euler rotations. In quantum mechanics, the rotation operator is given by $R_{\mathbf{n}}(\phi) = e^{-i\phi\mathbf{n}\cdot\mathbf{J}}$ to express a rotation through an angle ϕ about an arbitrary axis $\mathbf{n}$. Due to the rotational invariance, the operator H_o commutes with the rotation operators $\mathbf{J}$: $[H_o, \mathbf{J}] = 0$. The result of $[H_o, \mathbf{J}] = 0$ indicates that $[H_o, e^{-i\phi\mathbf{n}\cdot\mathbf{J}}] = 0$. The HG modes in Eq. (2) can be considered as the eigenstates along the J_3. The generalized eigenfunctions of H_o can be generated by performing the rotational transformation as[89]

$$\psi_{n_1,n_2}^{(\alpha,\beta)}(\tilde{x},\tilde{y}) = e^{-i\alpha J_3}\, e^{-i\beta J_2}\, \psi_{n_1,n_2}^{(\mathrm{HG})}(\tilde{x},\tilde{y}), \tag{6}$$

where α and β can be imaged as the azimuthal and polar angles for a point on the Poincaré sphere. The eigenfunctions $\psi_{n_1,n_2}^{(\alpha,\beta)}$ are named the HLG modes due to the property that they can be employed to link the HG modes to the LG modes by a continuously rotational transformation.

To expand the HLG mode $\psi_{n_1,n_2}^{(\alpha,\beta)}(\tilde{x},\tilde{y})$ with the basis of the HG modes $[\psi_{n_1,n_2}^{(\mathrm{HG})}(\tilde{x},\tilde{y})]$, the ladder operators are used to express the HG mode $\psi_{n_1,n_2}^{(\mathrm{HG})}(\tilde{x},\tilde{y})$ as

$$\psi_{n_1,n_2}^{(\mathrm{HG})}(\tilde{x},\tilde{y}) = \frac{(a_1^\dagger)^{n_1}}{\sqrt{n_1!}} \frac{(a_2^\dagger)^{n_2}}{\sqrt{n_2!}} \psi_{0,0}^{(\mathrm{HG})}(\tilde{x},\tilde{y}). \tag{7}$$

From Eqs. (6) and (7), the expansion of the HLG mode $\psi^{(\alpha,\beta)}_{n_1,n_2}(\tilde{x},\tilde{y})$ involves the property

$$e^{-i\alpha J_3}\, e^{-i\beta J_2}(a_1^\dagger)^{n_1} = (e^{-i\alpha J_3} e^{-i\beta J_2}\, a_1^\dagger\, e^{i\beta J_2} e^{i\alpha J_3})^{n_1} e^{-i\alpha J_3} e^{-i\beta J_2}. \quad (8)$$

Equation (8) can be further developed to obtain

$$e^{-i\alpha J_3}\, e^{-i\beta J_2}(a_1^\dagger)^{n_1}(a_2^\dagger)^{n_2} = (b_1^\dagger)^{n_1}(b_2^\dagger)^{n_2} e^{-i\alpha J_3} e^{-i\beta J_2}, \quad (9)$$

where

$$b_1^\dagger = e^{-i\alpha J_3} e^{-i\beta J_2}\, a_1^\dagger\, e^{i\beta J_2} e^{i\alpha J_3}, \quad (10)$$

$$b_2^\dagger = e^{-i\alpha J_3} e^{-i\beta J_2}\, a_2^\dagger\, e^{i\beta J_2} e^{i\alpha J_3}. \quad (11)$$

Using Eqs. (8)–(11) and

$$e^{-i\alpha J_3}\, e^{-i\beta J_2}\, \psi^{(\mathrm{HG})}_{0,0}(\tilde{x},\tilde{y}) = \psi^{(\mathrm{HG})}_{0,0}(\tilde{x},\tilde{y}), \quad (12)$$

the HLG modes can be derived as[80]

$$\psi^{(\alpha,\beta)}_{n_1,n_2}(\tilde{x},\tilde{y}) = \frac{(b_1^\dagger)^{n_1}}{\sqrt{n_1!}}\frac{(b_2^\dagger)^{n_2}}{\sqrt{n_2!}}\psi^{(\mathrm{HG})}_{0,0}(\tilde{x},\tilde{y}). \quad (13)$$

Note that Eq. (12) comes from the property of rotational invariance of ground state $\psi^{(\mathrm{HG})}_{0,0}(\tilde{x},\tilde{y})$. The ladder operators $b_1^\dagger$ and $b_2^\dagger$ can be explicitly given by

$$b_1^\dagger = a_1^\dagger\, e^{-i\alpha/2}\cos\left(\frac{\beta}{2}\right) + a_2^\dagger\, e^{i\alpha/2}\sin\left(\frac{\beta}{2}\right), \quad (14)$$

$$b_2^\dagger = -a_1^\dagger\, e^{-i\alpha/2}\sin\left(\frac{\beta}{2}\right) + a_2^\dagger\, e^{i\alpha/2}\cos\left(\frac{\beta}{2}\right). \quad (15)$$

Substituting Eqs. (14) and (15) into Eq. (13), the HLG modes are explicitly expanded as[88,89]

$$\psi^{(\alpha,\beta)}_{N-m,m}(\tilde{x},\tilde{y}) = e^{-iN\alpha/2}\sum_{s=0}^{N} e^{is\alpha}\, d^{\frac{N}{2}}_{\frac{N}{2}-s,\frac{N}{2}-m}(\beta)\,\psi^{(\mathrm{HG})}_{N-s,s}(\tilde{x},\tilde{y}), \quad (16)$$

where $N-m=n_1$, $m=n_2$, and the expansion coefficients $d^{\frac{N}{2}}_{\frac{N}{2}-s,\frac{N}{2}-m}$ are the Wigner d-matrix elements[90] given by

$$d^{\frac{N}{2}}_{\frac{N}{2}-s,\frac{N}{2}-m}(\beta) = \sum_{v=\max(0,m-s)}^{\min(m,N-s)}\left\{\frac{(-1)^v\sqrt{(N-m)!m!(N-s)!s!}}{(N-s-v)!v!(s-m+v)!(m-v)!} \times\left[\cos\left(\frac{\beta}{2}\right)\right]^{N-m+k-2s}\left[\sin\left(\frac{\beta}{2}\right)\right]^{m-k+2s}\right\}. \quad (17)$$

The expression of Wigner d-matrix elements $d^{\frac{N}{2}}_{\frac{N}{2}-s,\frac{N}{2}-m}$ in Eq. (17) is particularly important for calculating HLG modes straightforwardly.

Figure 1 shows the calculated patterns of HLG modes $\psi^{(\alpha,\beta)}_{n_1,n_2}(\tilde{x},\tilde{y})$ with $n_1=3$ and $n_2=8$ for various values of α and β. It can be seen that the HLG modes with $\alpha=0$ and $\beta=0$, i.e., along the J_3 axis, correspond to the HG modes $\psi^{(\mathrm{HG})}_{n_1,n_2}(\tilde{x},\tilde{y})$. On the other hand, the HLG modes with $\alpha=\pi/2$ and $\beta=\pi/2$, i.e., along the J_2 axis, correspond to the LG modes $\psi^{(\mathrm{LG})}_{n_1,n_2}(\tilde{x},\tilde{y})$. Note that the azimuthal quantum number of LG modes is determined by $l=n_2-n_1$ and the radial quantum number is given by the smaller of n_1 and n_2. In the J_1J_3 plane ($\alpha=0$), the HLG mode can be found to represent a continuous rotation of the HG mode from xy (0° and 90°) to diagonal (45° and 135°) symmetry by varying the angle of β from 0 to $\pi/2$. In the J_2J_3 plane ($\alpha=\pi/2$), the HLG mode represents a continuous transformation from the HG mode to the LG mode by varying the angle of β from 0 to $\pi/2$. In the J_1J_2 plane ($\beta=\pi/2$), the HLG mode represents a continuous transformation from the diagonal HG mode to the LG mode by varying the angle of β from 0 to $\pi/2$. The OAM per photon for the HLG mode $\psi^{(\alpha,\beta)}_{n_1,n_2}(\tilde{x},\tilde{y})$ can be analytically found to be given by $<L_z>=\hbar(n_1-n_2)\sin\alpha\sin\beta$. Except for $\alpha=0$, the HLG mode represents a feature of the traveling wave. By superposition between the HLG mode and its complex conjugate, the representation of the standing wave can be given by $\mathrm{Re}[\psi^{(\alpha,\beta)}_{n_1,n_2}(\tilde{x},\tilde{y})]$ as well as $\mathrm{Im}[\psi^{(\alpha,\beta)}_{n_1,n_2}(\tilde{x},\tilde{y})]$. The wave patterns of the standing HLG mode corresponding to the results in Fig. 1 are shown in Fig. 2. Note that the standing HLG modes are frequently observed in spherical laser cavities with symmetry breaking. Furthermore, the standing HLG modes are equivalent to the IG modes. The advantage of the HLG

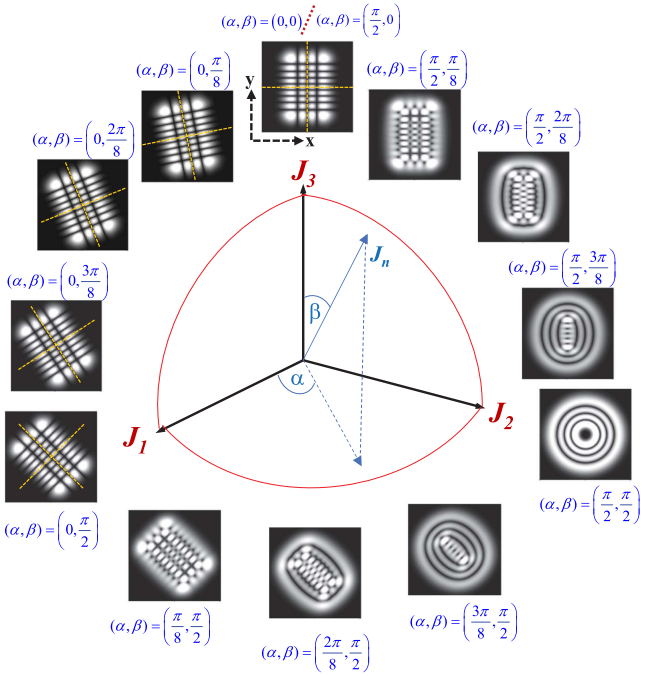

Fig. 1. Calculated patterns of HLG modes $\psi^{(\alpha,\beta)}_{n_1,n_2}(\tilde{x},\tilde{y})$ with $n_1=3$ and $n_2=8$ for various values of α and β on the Poincaré sphere.

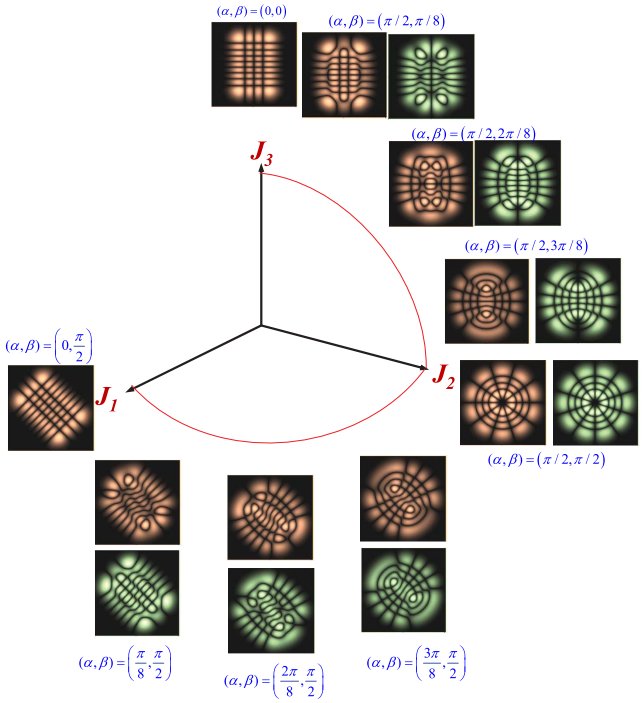

Fig. 2. Calculated patterns for the standing waves given by $\mathrm{Re}[\psi^{(\alpha,\beta)}_{n_1,n_2}(\tilde{x},\tilde{y})]$ (golden color) as well as $\mathrm{Im}[\psi^{(\alpha,\beta)}_{n_1,n_2}(\tilde{x},\tilde{y})]$ (green color), corresponding to the results in Fig. 1.

expression in Eq. (16) is analytical in terms of the Wigner d-matrix elements.

To begin with, it is introduced that the eigenmodes of the 1D quantum harmonic oscillator can be expressed as an integral of the 1D Gaussian wave-packet state over a trajectorial period. Then, this idea is extended to verify that the elliptical mode can be derived as an integral of the 2D Gaussian wave-packet state over the classical orbit by applying the inverse Fourier transform to the time-dependent coherent state of the 2D harmonic oscillator. The quantum Fourier transform is further used to derive that the HG mode can be completely expressed as a superposition of the elliptical modes, corresponding to a bundle of elliptical orbits.

Considering the 1D quantum harmonic oscillator with the natural frequency ω, the eigenfunctions in the 1D harmonic oscillator are given by

$$\begin{aligned}\Psi_n(\tilde{x},t) &= \psi_n(\tilde{x})e^{-i(n+1/2)\omega t}\\ &= \frac{1}{\sqrt{2^n n!\sqrt{\pi}}}H_n(\tilde{x})e^{-\tilde{x}^2/2}e^{-i(n+1/2)\omega t}.\end{aligned}\tag{18}$$

The generating function for the Hermite polynomials is given by[91]

$$e^{-\tau^2+2\tau\tilde{x}} = \sum_{n=0}^{\infty}\frac{\tau^n}{n!}H_n(\tilde{x}).\tag{19}$$

Note that the generating function is valid for all complex values of τ. Setting $\tau = u/\sqrt{2}$ and multiplying the term $e^{-(|u|^2+\tilde{x}^2)/2}$ on both sides of Eq. (19), after some rearrangement and in terms of $\psi_n(\tilde{x})$, the generating function can be used to express the Gaussian wave packet as

$$\begin{aligned}g(\tilde{x};u) &= \pi^{-1/4}e^{-(\tilde{x}^2-2\sqrt{2}u\tilde{x}+u^2+|u|^2)/2}\\ &= \sum_{n=0}^{\infty}\frac{u^n}{\sqrt{n!}}e^{-|u|^2/2}\psi_n(\tilde{x}).\end{aligned}\tag{20}$$

The representation of the wave function $g(\tilde{x};u)$ is related to Schrödinger's coherent state. Substituting $u=\sqrt{N}e^{-i(\omega t+\phi)}$ into Eq. (20), the wave function $g(\tilde{x};u)$ can be rewritten as

$$\begin{aligned}g(\tilde{x};u) &= \pi^{-1/4}e^{i\tilde{x}\sqrt{2}\,\mathrm{Im}(u)}e^{-i\mathrm{Re}(u)\mathrm{Im}(u)}e^{-[\tilde{x}-\sqrt{2}\mathrm{Re}(u)]^2/2}\\ &= e^{i\omega t/2}\sum_{n=0}^{\infty}\frac{N^{n/2}}{\sqrt{n!}}e^{-N/2}e^{-in\phi}\Psi_n(\tilde{x},t).\end{aligned}\tag{21}$$

This equation indicates that the wave function $g(\tilde{x};u)$ with $u=\sqrt{N}e^{-i(\omega t+\phi)}$ is the coherent superposition of all time-dependent eigenstates $\Psi_n(\tilde{x},t)$. Clearly, the intensity $|g(\tilde{x};u)|^2$ represents a Gaussian wave packet with the central peak to mimic the classical motion $\tilde{x}=\sqrt{2}\mathrm{Re}(u)=\sqrt{2N}\cos(\omega t+\phi)$, where the phase factor ϕ is related to the initial position.

Next, we discuss how to extract the eigenfunction $\psi_n(\tilde{x})$ from the Gaussian wave packet $g(\tilde{x};u)$ via the concept of the inverse Fourier transformation. For the sake of brevity, we substitute $u=\sqrt{N}e^{-i(\theta+\phi)}$ into Eq. (21) to obtain

$$\begin{aligned}g(\tilde{x};u) &= \pi^{-1/4}e^{-(\tilde{x}^2-2\sqrt{2}u\tilde{x}+u^2+|u|^2)/2}\\ &= \sum_{n=0}^{\infty}\frac{N^{n/2}}{\sqrt{n!}}e^{-N/2}e^{-in\phi}\psi_n(\tilde{x})e^{-in\theta},\end{aligned}\tag{22}$$

where the variable θ ranges from 0 to 2π. Using the orthogonal property where

$$\frac{1}{2\pi}\int_0^{2\pi}e^{i(n-n')\theta}\mathrm{d}\theta = \delta_{n,n'},\tag{23}$$

the inverse Fourier transformation with $u=\sqrt{N}e^{-i\theta}$ can lead to

$$\frac{1}{2\pi}\int_0^{2\pi}g(\tilde{x};u)e^{iN\theta}\mathrm{d}\theta = \frac{N^{n/2}}{\sqrt{N!}}e^{-N/2}\psi_N(\tilde{x}).\tag{24}$$

Consequently, the eigenfunctions $\psi_n(\tilde{x})$ with $n=N$ can be expressed as

$$\psi_N(\tilde{x}) = \frac{\sqrt{N!}\,\pi^{-1/4}}{N^{n/2}e^{-N/2}}\left(\frac{1}{2\pi}\int_0^{2\pi}e^{-\frac{\tilde{x}^2-2\sqrt{2}u\tilde{x}+u^2+|u|^2}{2}}e^{iN\theta}\mathrm{d}\theta\right).\tag{25}$$

Equation (25) is exact for calculating the eigenfunctions $\psi_N(\tilde{x})$ for any order N. Although the inverse extraction is straightforward in the 1D harmonic oscillator, the extension to the 2D or higher-dimensional systems can

provide an important insight into the connection between the quantum eigenstates and classical periodic orbits.

In classical mechanics, the general periodic orbits in the 2D isotropic harmonic oscillator are the elliptical orbits. To construct the complete quantum-classical correspondence, we apply Schrödinger's coherent state to the 2D harmonic oscillator to derive an integral representation for the elliptical mode related to the classical trajectory manifestly. Exploiting Schrödinger's coherent state in Eq. (20) and the separable property, the time-dependent coherent state for the 2D harmonic oscillator can be expressed as[80,87]

$$g(\tilde{x},\tilde{y},u_1,u_2)=\frac{1}{\sqrt{\pi}}e^{-\frac{\tilde{x}^2-2\sqrt{2}u_1\tilde{x}+u_1^2+|u_1|^2}{2}}e^{-\frac{\tilde{y}^2-2\sqrt{2}u_2\tilde{y}+u_2^2+|u_2|^2}{2}}$$
$$=\sum_{n_1=0}^{\infty}\sum_{n_2=0}^{\infty}\frac{{u_1}^{n_1}}{\sqrt{n_1!}}\frac{{u_2}^{n_2}}{\sqrt{n_2!}}e^{-\frac{|u_1|^2+|u_2|^2}{2}}\psi^{(\mathrm{HG})}_{n_1,n_2}(\tilde{x},\tilde{y}), \tag{26}$$

where $u_1=\sqrt{N_1}e^{-i(\omega t+\phi_1)}$, $u_2=\sqrt{N_2}e^{-i(\omega t+\phi_2)}$, N_1, and N_2 are related to the oscillation amplitude, and ϕ_1 and ϕ_2 are related to the initial position. Clearly, the Gaussian wave-packet state $g(\tilde{x},\tilde{y},u_1,u_2)$ in Eq. (26) can reveal the time-dependent quantum-classical correspondence.

Since the ellipticity of the classical orbit depends only on the relative phase between ϕ_1 and ϕ_2, the parameters u_1 and u_2 are conveniently expressed as

$$\begin{bmatrix}u_1\\u_2\end{bmatrix}=\begin{bmatrix}\sqrt{N_1}e^{-i(\theta+\phi/2)}\\\sqrt{N_2}e^{-i(\theta-\phi/2)}\end{bmatrix}, \tag{27}$$

where the variable θ ranges from 0 to 2π, and the phase factor ϕ determines the ellipticity. Substituting Eq. (27) into Eq. (26), the wave function $g(\tilde{x},\tilde{y},u_1,u_2)$ can be rewritten as

$$g(\tilde{x},\tilde{y},u_1,u_2)$$
$$=\frac{1}{\sqrt{\pi}}e^{-\frac{\tilde{x}^2-2\sqrt{2}u_1\tilde{x}+u_1^2+|u_1|^2}{2}}e^{-\frac{\tilde{y}^2-2\sqrt{2}u_2\tilde{y}+u_2^2+|u_2|^2}{2}}$$
$$=\sum_{n_1=0}^{\infty}\sum_{n_2=0}^{\infty}\frac{N_1^{\frac{n_1}{2}}}{\sqrt{n_1!}}\frac{N_2^{\frac{n_2}{2}}}{\sqrt{n_2!}}e^{-\frac{N_1+N_2}{2}}\psi^{(\mathrm{HG})}_{n_1,n_2}(\tilde{x},\tilde{y})e^{-i(n_1+n_2)\theta}$$
$$\times e^{-i(n_1-n_2)\phi/2}. \tag{28}$$

The wave function $g(\tilde{x},\tilde{y},u_1,u_2)$ is the time-dependent coherent state that can be expressed as the superposition of the stationary coherent states with different eigenvalues n_1+n_2. By using the inverse Fourier transform and Eq. (23), the stationary coherent state with eigenvalue $n_1+n_2=N_1+N_2$ can be expressed as an integral form[80]:

$$\Phi_{N_1,N_2}(\tilde{x},\tilde{y},\phi)=\frac{1}{2\pi}\int_0^{2\pi}g(\tilde{x},\tilde{y},u_1,u_2)e^{i(N_1+N_2)\theta}\mathrm{d}\theta. \tag{29}$$

Exploiting the new index K to specify the group of the degenerate HG modes $\psi^{(\mathrm{HG})}_{n_1,n_2}(\tilde{x},\tilde{y})$ with $n_1=N_1-K$ and $n_2=N_2+K$, the stationary coherent state $\Phi_{N_1,N_2}(\tilde{x},\tilde{y},\phi)$ can be derived as

$$\Phi_{N_1,N_2}(\tilde{x},\tilde{y},\phi)$$
$$=\frac{1}{2\pi}\int_0^{2\pi}\frac{1}{\sqrt{\pi}}e^{-\frac{\tilde{x}^2-2\sqrt{2}u_1\tilde{x}+u_1^2+|u_1|^2}{2}}e^{-\frac{\tilde{y}^2-2\sqrt{2}u_2\tilde{y}+u_2^2+|u_2|^2}{2}}e^{i(N_1+N_2)\theta}\mathrm{d}\theta$$
$$=\sum_{K=-N_2}^{N_1}\left\{\frac{N_1^{(N_1-K)/2}}{\sqrt{(N_1-K)!}}\frac{N_2^{(N_2+K)/2}}{\sqrt{(N_2+K)!}}e^{-\frac{N_1+N_2}{2}}\right.$$
$$\left.\times e^{-i(N_1-N_2)\phi/2}\psi^{(\mathrm{HG})}_{N_1-K,N_2+K}(\tilde{x},\tilde{y})e^{iK\phi}\right\}. \tag{30}$$

For a given (N_1,N_2,ϕ), the spatial intensity of the stationary coherent state $\Phi_{N_1,N_2}(\tilde{x},\tilde{y},\phi)$ is exactly concentrated on the elliptical orbit. The summation expression in Eq. (30) is exactly the same as the representation of the SU(2) coherent state[76,79] that is calculated by using N_1+N_2+1 degenerate HG modes $\psi^{(\mathrm{HG})}_{N_1-K,N_2+K}(\tilde{x},\tilde{y})$. Here, we remarkably verify that the stationary coherent state $\Phi_{N_1,N_2}(\tilde{x},\tilde{y},\phi)$ can be expressed as an integral of the Gaussian wave-packet state over a trajectorial period. The numerical computation in Eq. (30) can be simply and efficiently performed without the need of calculating HG modes $\psi^{(\mathrm{HG})}_{N_1-K,N_2+K}(\tilde{x},\tilde{y})$. More importantly, the quantum-classical correspondence can be manifested in the Gaussian wave-packet state in Eq. (30).

The discrete Fourier transform $\{F_0,F_1,\cdots,F_N\}$ of a discrete function $\{f_0,f_1,\cdots,f_N\}$ and its inverse are given by[92]

$$F_k=\frac{1}{N+1}\sum_{n=0}^{N}f_n e^{-i2\pi nk/(N+1)}, \tag{31}$$

$$f_n=\sum_{k=0}^{N}F_k e^{i2\pi nk/(N+1)}. \tag{32}$$

The quantum Fourier transform is a discrete Fourier transform upon the quantum state. From Eq. (30), it can be found that the stationary coherent state $\Phi_{N_1,N_2}(\tilde{x},\tilde{y},\phi)$ consists of N_1+N_2+1 degenerate HG modes $\psi^{(\mathrm{HG})}_{N_1-K,N_2+K}(\tilde{x},\tilde{y})$, with the weighting coefficient including the relative phase term $e^{iK\phi}$. For the case $N_1+N_2=N$, we can use the concept of the discrete Fourier transform to divide the phase factor ϕ into $N+1$ different values as $\phi_n=2\pi n/(N+1)$ with $n=0,1,\cdots,N$. Based on Eqs. (31) and (32), the set $\{\Phi_{N_1,N_2}(\tilde{x},\tilde{y},\phi_n)\}$ is a complete basis that can be employed to represent the degenerate HG mode $\psi^{(\mathrm{HG})}_{N_1-K,N_2+K}(\tilde{x},\tilde{y})$ by means of the inverse quantum Fourier transform. The inverse Fourier transform for Eq. (30) can be derived as

$$\frac{N_1^{(N_1-K)/2}}{\sqrt{(N_1-K)!}}\frac{N_2^{(N_2+K)/2}}{\sqrt{(N_2+K)!}}e^{-\frac{N_1+N_2}{2}}\psi^{(\mathrm{HG})}_{N_1-K,N_2+K}(\tilde{x},\tilde{y})$$
$$=\frac{1}{N+1}\sum_{n=0}^{N}\Phi_{N_1,N_2}(\tilde{x},\tilde{y},\phi_n)e^{i(N_1-N_2-2K)\phi_n/2}. \tag{33}$$

Without loss of generality, we can use Eq. (33) for $K = 0$ to express the HG mode $\psi^{(\mathrm{HG})}_{N_1,N_2}(\tilde{x},\tilde{y})$ as

$$\psi^{(\mathrm{HG})}_{N_1,N_2}(\tilde{x},\tilde{y}) = C_{N_1,N_2}\frac{1}{N+1}\sum_{n=0}^{N}\Phi_{N_1,N_2}(\tilde{x},\tilde{y},\phi_n)e^{i(N_1-N_2)\phi_n/2}, \quad (34)$$

where

$$C_{N_1,N_2} = \left(\frac{N_1^{N_1/2}}{\sqrt{N_1!}}\frac{N_2^{N_2/2}}{\sqrt{N_2!}}e^{-\frac{N_1+N_2}{2}}\right)^{-1}. \quad (35)$$

Equation (34) indicates that the HG mode $\psi^{(\mathrm{HG})}_{N_1,N_2}(\tilde{x},\tilde{y})$ can be interpreted as a summation of the generalized elliptical modes $\Phi_{N_1,N_2}(\tilde{x},\tilde{y},\phi_n)$, which are given by an integral of the Gaussian wave-packet state over the classical orbit, as shown in Eq. (30). More remarkably, Eq. (34) provides a general expression for the HG mode $\psi^{(\mathrm{HG})}_{N_1,N_2}(\tilde{x},\tilde{y})$ without involving the Hermite polynomials.

Figure 3 shows the calculated results for $\psi^{(\mathrm{HG})}_{N_1,N_2}(\tilde{x},\tilde{y})$ and $\Phi_{N_1,N_2}(\tilde{x},\tilde{y},\phi_n)$ by using Eqs. (30) and (34) with $(N_1,N_2) = (3,4)$. The superposed elliptical modes $\Phi_{N_1,N_2}(\tilde{x},\tilde{y},\phi_n)$ can be seen to have different ellipticities and different directions for the major axes.

Figures 4 and 5 show the calculated results for the higher modes with $(N_1,N_2) = (7,8)$ and $(N_1,N_2) = (3,12)$. The range for the ellipticities of the superposed elliptical modes $\Phi_{N_1,N_2}(\tilde{x},\tilde{y},\phi_n)$ can be found to be consistent with the shape of the spatial pattern $|\psi^{(\mathrm{HG})}_{N_1,N_2}(\tilde{x},\tilde{y})|$. In addition to the HG modes, the same approach based on the generalized elliptical modes can be exploited to represent the generalized HLG modes. Replacing the HG modes $\psi^{(\mathrm{HG})}_{n_1,n_2}(\tilde{x},\tilde{y})$ with HLG modes $\psi^{(\alpha,\beta)}_{n_1,n_2}(\tilde{x},\tilde{y})$ in Eq. (26), the HLG-based coherent state is given by[80,87]

$$g^{(\alpha,\beta)}(\tilde{x},\tilde{y},u_1,u_2) = \sum_{n_1=0}^{\infty}\sum_{n_2=0}^{\infty}\frac{u_1^{n_1}}{\sqrt{n_1!}}\frac{u_2^{n_2}}{\sqrt{n_2!}}e^{-\frac{|u_1|^2+|u_2|^2}{2}}\psi^{(\alpha,\beta)}_{n_1,n_2}(\tilde{x},\tilde{y}). \quad (36)$$

By using the ladder operators, the coherent state $\tilde{g}^{(\alpha,\beta)}(\tilde{x},\tilde{y},u_1,u_2)$ can also be derived as a Gaussian wave-packet state moving in the elliptical trajectory. Substituting Eq. (11) into Eq. (36), the coherent state $g^{(\alpha,\beta)}(\tilde{x},\tilde{y},u_1,u_2)$ can be expressed as

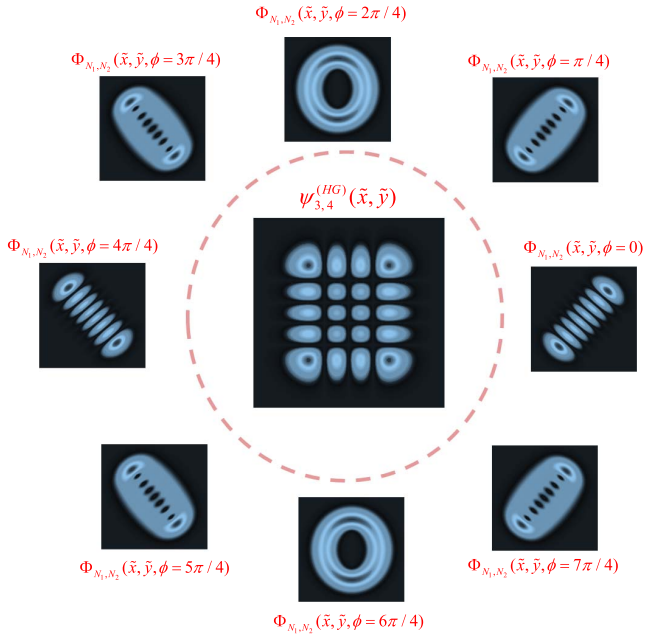

Fig. 3. Calculated results for $\psi^{(\mathrm{HG})}_{N_1,N_2}(\tilde{x},\tilde{y})$ and $\Phi_{N_1,N_2}(\tilde{x},\tilde{y},\phi_n)$ by using Eqs. (30) and (34) with $(N_1,N_2) = (3,4)$.

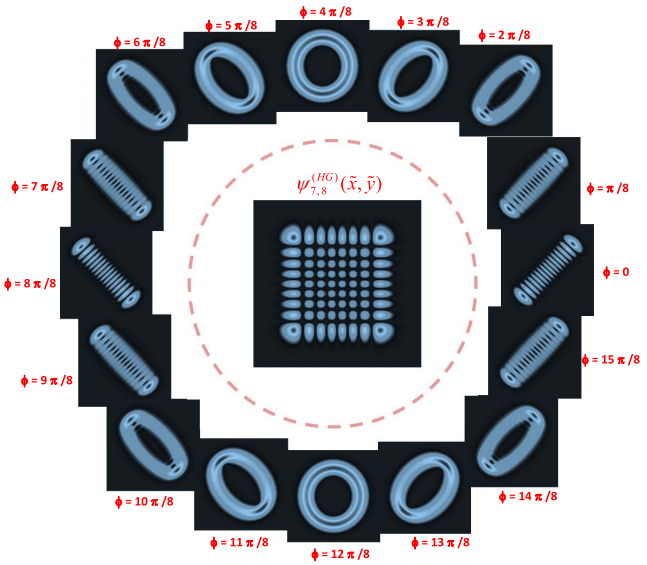

Fig. 4. Calculated results for $\psi^{(\mathrm{HG})}_{N_1,N_2}(\tilde{x},\tilde{y})$ and $\Phi_{N_1,N_2}(\tilde{x},\tilde{y},\phi_n)$ by using Eqs. (30) and (34) with $(N_1,N_2) = (7,8)$.

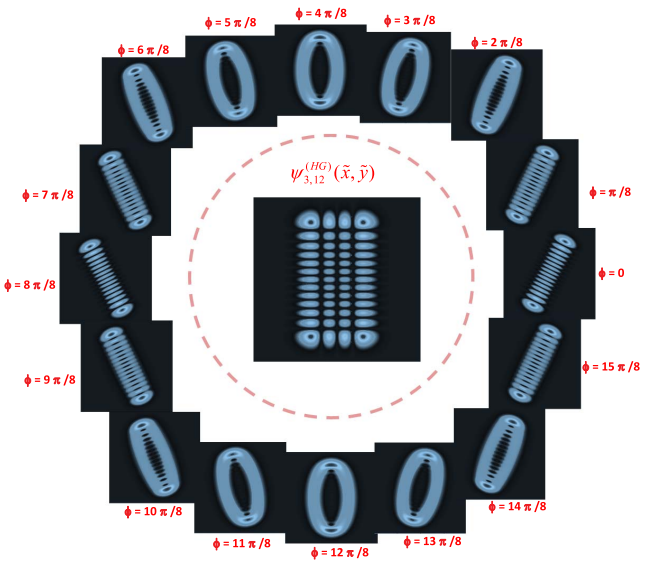

Fig. 5. Calculated results for $\psi^{(\mathrm{HG})}_{N_1,N_2}(\tilde{x},\tilde{y})$ and $\Phi_{N_1,N_2}(\tilde{x},\tilde{y},\phi_n)$ by using Eqs. (30) and (34) with $(N_1,N_2) = (3,12)$.

$$g^{(\alpha,\beta)}(\tilde{x},\tilde{y},u_1,u_2) = \sum_{n_1=0}^{\infty}\sum_{n_2=0}^{\infty}\frac{u_1^{n_1}}{n_1!}\frac{u_2^{n_2}}{n_2!}e^{-(|u_1|^2+|u_2|^2)/2}(b_1^{\dagger})^{n_1}(b_2^{\dagger})^{n_2}\psi_{0,0}(\tilde{x},\tilde{y}). \tag{37}$$

The product of the infinite double series in Eq. (37) can be simplified as a single infinite summation by rearranging with $n_1+n_2=N$. The result is given by

$$g^{(\alpha,\beta)}(\tilde{x},\tilde{y},u_1,u_2) = \sum_{N=0}^{\infty} e^{-\frac{|u_1|^2+|u_2|^2}{2}}\frac{(u_1 b_1^{\dagger}+u_2 b_2^{\dagger})^N}{N!}\psi_{0,0}^{(\mathrm{HG})}(\tilde{x},\tilde{y}). \tag{38}$$

Using Eqs. (14) and (15) to replace $b_1^{\dagger}$ and $b_2^{\dagger}$ with $a_1^{\dagger}$ and $a_2^{\dagger}$, the coherent state $g^{(\alpha,\beta)}(\tilde{x},\tilde{y},u_1,u_2)$ can be rewritten as

$$g^{(\alpha,\beta)}(\tilde{x},\tilde{y},u_1,u_2) = \sum_{N=0}^{\infty} e^{-\frac{|v_1|^2+|v_2|^2}{2}}\frac{(v_1 a_1^{\dagger}+v_2 a_2^{\dagger})^N}{N!}\psi_{0,0}^{(\mathrm{HG})}(\tilde{x},\tilde{y}), \tag{39}$$

where the transformation between (u_1,u_2) and (v_1,v_2) is given by

$$\begin{bmatrix} v_1 \\ v_2 \end{bmatrix} = \begin{bmatrix} e^{-i\alpha/2}\cos\left(\frac{\beta}{2}\right) & -e^{-i\alpha/2}\sin\left(\frac{\beta}{2}\right) \\ e^{i\alpha/2}\sin\left(\frac{\beta}{2}\right) & e^{i\alpha/2}\cos\left(\frac{\beta}{2}\right) \end{bmatrix}\begin{bmatrix} u_1 \\ u_2 \end{bmatrix}. \tag{40}$$

By expressing the summation in Eq. (39) back to the product of the infinite double series, the coherent state $g^{(\alpha,\beta)}(\tilde{x},\tilde{y},u_1,u_2)$ can be written as

$$g^{(\alpha,\beta)}(\tilde{x},\tilde{y},u_1,u_2) = \sum_{m_1=0}^{\infty}\sum_{m_2=0}^{\infty}\frac{v_1^{m_1}}{m_1!}\frac{v_2^{m_2}}{m_2!}e^{-(|v_1|^2+|v_2|^2)/2}(a_1^{\dagger})^{m_1}(a_2^{\dagger})^{m_2}\psi_{0,0}^{(\mathrm{HG})}(\tilde{x},\tilde{y}). \tag{41}$$

From Eq. (26), the coherent state $g^{(\alpha,\beta)}(\tilde{x},\tilde{y},u_1,u_2)$ in Eq. (41) can be analytically given by

$$g^{(\alpha,\beta)}(\tilde{x},\tilde{y},u_1,u_2) = \frac{1}{\sqrt{\pi}}e^{-\frac{\tilde{x}^2-2\sqrt{2}v_1\tilde{x}+v_1^2+|v_1|^2}{2}}e^{-\frac{\tilde{y}^2-2\sqrt{2}v_2\tilde{y}+v_2^2+|v_2|^2}{2}}. \tag{42}$$

Equation (42) indicates that $g^{(\alpha,\beta)}(\tilde{x},\tilde{y},u_1,u_2)$ is a Gaussian wave packet with the central peak moving in the elliptical orbit of $\tilde{x}=\sqrt{2}\mathrm{Re}(v_1)$ and $\tilde{y}=\sqrt{2}\mathrm{Re}(v_2)$. The stationary elliptical mode derived from the wave packet $g^{(\alpha,\beta)}(\tilde{x},\tilde{y},u_1,u_2)$ can be given by

$$\Phi_{N_1,N_2}^{(\alpha,\beta)}(\tilde{x},\tilde{y},\phi) = \frac{1}{2\pi}\int_0^{2\pi} g^{(\alpha,\beta)}(\tilde{x},\tilde{y},u_1,u_2)e^{i(N_1+N_2)\theta}\mathrm{d}\theta. \tag{43}$$

The OAM per photon for the elliptical orbital mode $\Phi_{N_1,N_2}^{(\alpha,\beta)}(\tilde{x},\tilde{y},\phi)$ can be found to be

$$<L_z> = \hbar[(n_1-n_2)\sin\alpha\sin\beta + 2\sqrt{n_1 n_2}(\cos\alpha\sin\phi+\cos\beta\sin\alpha\cos\phi)]. \tag{44}$$

Following the derivation given in Eqs. (33)–(35), the HLG mode $\psi_{N_1,N_2}^{(\mathrm{HLG})}(\tilde{x},\tilde{y})$ can be derived as

$$\psi_{N_1,N_2}^{(\alpha,\beta)}(\tilde{x},\tilde{y}) = C_{N_1,N_2}\frac{1}{N+1}\sum_{n=0}^{N}\Phi_{N_1,N_2}^{(\alpha,\beta)}(\tilde{x},\tilde{y},\phi_n)e^{i(N_1-N_2)\phi_n/2}. \tag{45}$$

Equation (45) indicates that the HLG mode $\Psi_{N_1,N_2}^{(\alpha,\beta)}(\tilde{x},\tilde{y})$ can be interpreted as a superposition of the generalized elliptical modes $\Phi_{N_1,N_2}^{(\alpha,\beta)}(\tilde{x},\tilde{y},\phi)$, corresponding to a bundle of elliptical orbits.

The numerical demonstration is the modes $\Phi_{N_1,N_2}^{(\alpha,\beta)}(\tilde{x},\tilde{y},\phi_n)$ with $\alpha=\pi/2$ and $\beta=\pi/2$. For this case, the mode $\psi_{N_1,N_2}^{(\alpha,\beta)}(\tilde{x},\tilde{y})$ is the LG mode $\psi_{N_1,N_2}^{(\mathrm{LG})}(\tilde{x},\tilde{y})$.

Figure 6 shows the calculated results for $\Phi_{N_1,N_2}^{(\alpha,\beta)}(\tilde{x},\tilde{y},\phi_n)$ by using the integral formula in Eqs. (42) and (43) with $(N_1,N_2)=(3,12)$, $(\alpha,\beta)=(\pi/2,\pi/2)$, and $\phi_n=\pi n/8$ with $n=0,1,\cdots,15$. The calculated elliptical modes $\Phi_{N_1,N_2}^{(\alpha,\beta)}(\tilde{x},\tilde{y},\phi_n)$ with $(\alpha,\beta)=(\pi/2,\pi/2)$ can be seen to have different directions for the major axes, but their ellipticities are the same. Applying the calculated $\Phi_{N_1,N_2}^{(\alpha,\beta)}(\tilde{x},\tilde{y},\phi_n)$ to Eq. (45), the resulting pattern for $\psi_{N_1,N_2}^{(\alpha,\beta)}(\tilde{x},\tilde{y})$, as shown in the central part of Fig. 6, can be seen to be the LG mode $\psi_{N_1,N_2}^{(\mathrm{LG})}(\tilde{x},\tilde{y})$. Both $\psi_{N_1,N_2}^{(\mathrm{LG})}(\tilde{x},\tilde{y})$ and $\Phi_{N_1,N_2}^{(\alpha,\beta)}(\tilde{x},\tilde{y},\phi_n)$ are the features of the traveling waves. The representation of the standing waves can be given

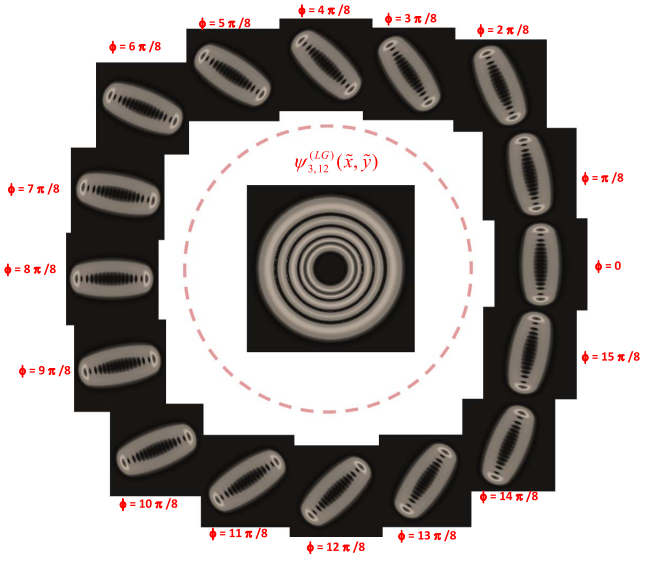

Fig. 6. Calculated results for $\psi_{N_1,N_2}^{(\mathrm{LG})}(\tilde{x},\tilde{y})$ and $\Phi_{N_1,N_2}^{(\alpha,\beta)}(\tilde{x},\tilde{y},\phi_n)$ by using Eqs. (43) and (45) with $(\alpha,\beta)=(\pi/2,\pi/2)$ and $(N_1,N_2)=(3,12)$.

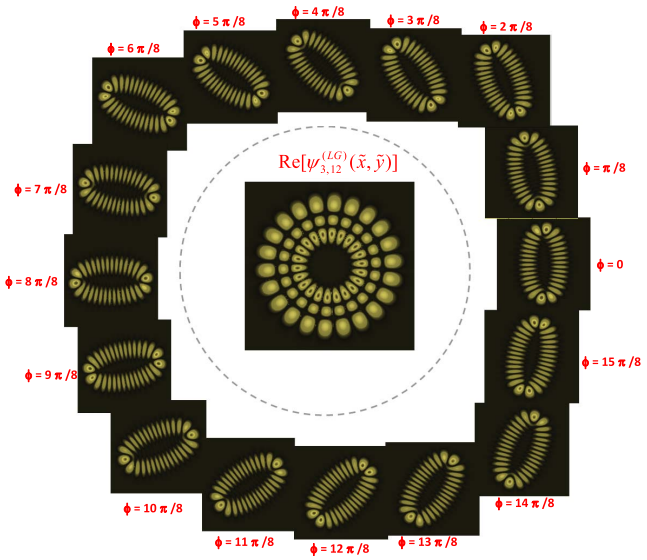

Fig. 7. Calculated results for the standing waves of $\mathrm{Re}[\psi^{(\mathrm{LG})}_{N_1,N_2}(\tilde{x},\tilde{y})]$ and $\mathrm{Re}[\Phi^{(\alpha,\beta)}_{N_1,N_2}(\tilde{x},\tilde{y},\phi_n)]$ corresponding to the traveling wave shown in Fig. 6.

by $\mathrm{Re}[\psi^{(\mathrm{LG})}_{N_1,N_2}(\tilde{x},\tilde{y})]$ and $\mathrm{Im}[\psi^{(\mathrm{LG})}_{N_1,N_2}(\tilde{x},\tilde{y})]$, which are superposed by $\mathrm{Re}[\Phi^{(\alpha,\beta)}_{N_1,N_2}(\tilde{x},\tilde{y},\phi_n)]$ and $\mathrm{Im}[\Phi^{(\alpha,\beta)}_{N_1,N_2}(\tilde{x},\tilde{y},\phi_n)]$.

The calculated results for the standing waves $\mathrm{Re}[\psi^{(\mathrm{LG})}_{N_1,N_2}(\tilde{x},\tilde{y})]$ with $(N_1,N_2)=(3,12)$ are shown in Fig. 7.

Figure 8 shows the case for the calculated results with $(N_1,N_2)=(4,11)$, $(\alpha,\beta)=(2\pi/5,2\pi/5)$, and $\phi_n=\pi n/8$ with $n=0,1,\cdots,15$. The calculated elliptical modes $\Phi^{(\alpha,\beta)}_{N_1,N_2}(\tilde{x},\tilde{y},\phi_n)$ with $(\alpha,\beta)=(2\pi/5,2\pi/5)$ can be seen to have different ellipticities and different directions for the major axes.

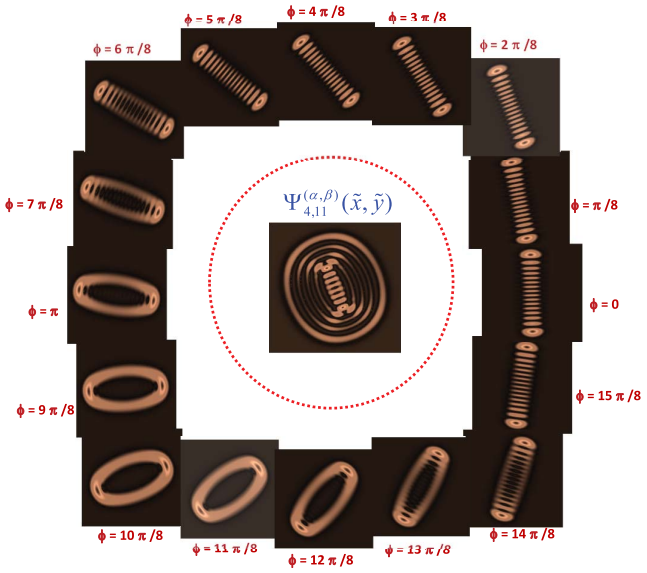

Fig. 8. Calculated results for $\psi^{(\alpha,\beta)}_{N_1,N_2}(\tilde{x},\tilde{y})$ and $\Phi^{(\alpha,\beta)}_{N_1,N_2}(\tilde{x},\tilde{y},\phi_n)$ by using Eqs. (43) and (45) with $(\alpha,\beta)=(2\pi/5,2\pi/5)$ and $(N_1,N_2)=(4,11)$.

Abramochkin and Volostnikov originally used an AMC formed by a matched pair of cylindrical lenses to generate the so-called HLG beams[69]. The HLG beams, a continuous evolution between HG and LG beams, can successively be realized by rotating the cylindrical lens about the optical axis by an angle ζ, as depicted in Fig. 9. The LG modes are just the HLG modes with $\zeta=\pi/4$. The HLG modes in the successive transformation lying between the HG and LG modes display a plentiful evolution of point dislocations and edge dislocations. The AMC mode converter was later used to generate the light fields with nonzero OAM[68]. The traditional AMC needs two precisely spaced and aligned cylindrical lenses[68,69]. A modified AMC based on a single cylindrical lens was discovered to generate the optical vortex beams more quickly and effectively[93,94]. Here, we make a review to theoretically characterize the propagation evolution of the vortex structures of HG beams transformed by a single lens AMC with an arbitrary angle[8].

The laser beam corresponding to the HG mode with the transverse indices of m and n in the forward propagation is given by[3,4]

$$\begin{aligned}\Psi^{(\mathrm{HG})}_{n,m}(x,y,z)&=\psi^{(\mathrm{HG})}_{n,m}(\tilde{x},\tilde{y})\,e^{-i(n+1/2)\theta_{G,x}(z)}\,e^{-i(m+1/2)\theta_{G,y}(z)}\\&\quad\times e^{ikx^2/2R_x(z)}\,e^{iky^2/2R_y(z)},\end{aligned}\tag{46}$$

where $\tilde{x}=\sqrt{2}x/w_x(z)$, $\tilde{y}=\sqrt{2}y/w_y(z)$, $w_x(z)$, and $w_y(z)$ are the beam radii, $\theta_{G,x}(z)$ and $\theta_{G,y}(z)$ are the Gouy phases, and $R_x(z)$ and $R_y(z)$ are the wavefront curvatures. The configuration for creating a vortex beam from an HG beam with a single cylindrical lens is shown in Fig. 9(a). The key feature is that a spherical lens is used to focus the input HG beam to have a new waist at a distance f just ahead of a cylindrical lens with focal length f and a new Rayleigh range z_R equal to f. To derive the HG beam transformed by a single lens AMC with arbitrary angle ζ, the eigenfunction basis needs to change from the xy-Cartesian coordinate system to the $x'y'$-Cartesian coordinate system in which the origin is kept fixed and the x' and y' axes are the active and inactive components,

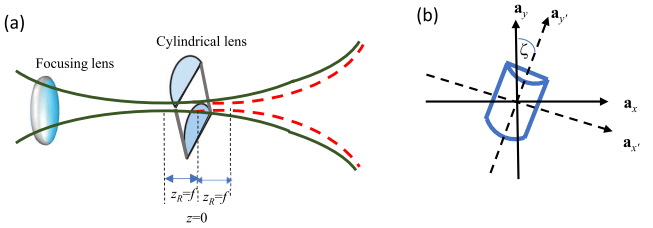

Fig. 9. (a) Configuration of the single lens mode converter. Two vertical lines show the positions of the beam waists produced by the spherical matching lens and by the active axis of the cylindrical lens with focal length f. (b) Relationship between the xy-Cartesian coordinate system and the $x'y'$-Cartesian coordinate system. The x' and y' axes are the active and inactive components of the cylindrical lens.

respectively, as shown in Fig. 9(b). The original coordinates (x, y) of a point Q are related to its new coordinates (x', y') by

$$\begin{pmatrix} \tilde{x}' \\ \tilde{y}' \end{pmatrix} = \begin{pmatrix} \cos\zeta & -\sin\zeta \\ \sin\zeta & \cos\zeta \end{pmatrix} \begin{pmatrix} \tilde{x} \\ \tilde{y} \end{pmatrix}. \tag{47}$$

In terms of Wigner d coefficients in Eq. (17), the $\psi^{(\mathrm{HG})}_{N-m,m}(\tilde{x}, \tilde{y})$ can be expanded with the basis $\psi^{(\mathrm{HG})}_{N-s,s}(\tilde{x}', \tilde{y}')$ as[8]

$$\psi^{(\mathrm{HG})}_{N-m,m}(\tilde{x}, \tilde{y}) = \sum_{s=0}^{N} d^{\frac{N}{2}}_{\frac{N}{2}-s,\frac{N}{2}-m}(2\zeta)\psi^{(\mathrm{HG})}_{N-s,s}(\tilde{x}', \tilde{y}'). \tag{48}$$

The arrangement shown in Fig. 9(a) is used to consider the effects of the cylindrical lens in the region of $z > 0$. The beam waists in the x' (active) and y' (inactive) axes are separable and given by

$$w_{x'}(z) = w_o\sqrt{1 + [(z - z_R)/z_R]^2}, \tag{49}$$

$$w_{y'}(z) = w_o\sqrt{1 + [(z + z_R)/z_R]^2}. \tag{50}$$

Note that z_R is equal to the focal length f of the cylindrical lens in the AMC configuration. In addition, the Gouy phases in the x' (active) and y' (inactive) axes are different and given by

$$\theta_{G,x'}(z) = \frac{\pi}{2} + \arctan\,[(z - z_R)/z_R], \tag{51}$$

$$\theta_{G,y'}(z) = \arctan\,[(z + z_R)/z_R]. \tag{52}$$

The wavefront curvatures in the x' (active) and y' (inactive) axes are also different and given by

$$\frac{1}{R_{x'}(z)} = \frac{z - z_R}{(z - z_R)^2 + z_R^2}, \tag{53}$$

$$\frac{1}{R_{y'}(z)} = \frac{z + z_R}{(z + z_R)^2 + z_R^2}. \tag{54}$$

Using Eqs. (49)–(54) to characterize the phase variation for each state $\psi^{(\mathrm{HG})}_{N-s,s}(\tilde{x}', \tilde{y}')$ in Eq. (48), the wave function for the HG beam transformed by a single lens AMC with arbitrary angle ζ in the propagation evolution can be derived as[8]

$$\Psi_{N-m,m}(x, y, z; \zeta) = e^{-i[(N+1/2)\theta_{G,y'}(z)+\theta_{G,x'}(z)/2]}\psi^{(\alpha,\beta)}_{N-m,m}(\tilde{x}', \tilde{y}')e^{i\Omega(\tilde{x}',\tilde{y}',z)}, \tag{55}$$

where $\tilde{x}' = \sqrt{2}x'/w_{x'}(z)$, $\tilde{y}' = \sqrt{2}y'/w_{y'}(z)$, $\beta = 2\zeta$, $\alpha(z) = \theta_{G,x'}(z) - \theta_{G,y'}(z)$, and

$$\Omega(\tilde{x}', \tilde{y}', z) = \frac{1}{2z_R}[z(\tilde{x}'^2 + \tilde{y}'^2) - z_R(\tilde{x}'^2 - \tilde{y}'^2)]. \tag{56}$$

Using Eqs. (51) and (52), the Gouy phase difference $\alpha(z)$ can be found to increase from 0 to $\pi/2$ for z from 0 to ∞. The wave pattern of the converted beam $\Psi_{N-m,m}(x, y, z; \zeta)$ is exclusively determined by the wave function $\psi^{(\alpha,\beta)}_{N-m,m}(\tilde{x}', \tilde{y}')$ in Eq. (55). The representation of $\Psi_{N-m,m}(x, y, z; \zeta)$ can be related to the SU(2) transform for the HG mode $\psi^{(\mathrm{HG})}_{N-s,s}(\tilde{x}', \tilde{y}')$ given in Eq. (16). Furthermore, the converted beam $\Psi_{N-m,m}(x, y, z; \zeta)$ in the far field $z \to \infty$ with ζ changing from 0 to $\pi/4$ is associated with the HLG beam to be transformed from the HG to the LG beam. Specifically, the beam $\Psi_{N-m,m}(x, y, z \to \infty; \zeta)$ corresponds to the HG and LG modes for $\zeta = 0$ and $\zeta = \pi/4$, respectively. On the other hand, the phase functions $\Omega(\tilde{x}', \tilde{y}', z)$ in Eq. (56) resulting from the wavefront curvatures in Eqs. (53) and (54) do not involve the overall wave patterns of the converted beams $\Psi_{N-m,m}(x, y, z; \zeta)$, but significantly affect their phase structures in the propagation. It has been demonstrated that the HG modes can be straightforwardly generated from an off-axis end-pumped Nd-doped vanadate laser[5,8]. The laser cavity configuration is a simple concave-plano resonator. The laser medium is an a-cut 0.2 at.% Nd:YVO_4 crystal with both side coated for antireflection at 1064 nm. The pump source was a 2.5 W 808 nm fiber-coupled laser diode with a core diameter of 100 μm and a numerical aperture of 0.16. Further detailed descriptions for the experimental setup can be found in the previous papers[5,8].

In the following, we exploit the derived formula to analyze the vortex beams that are generated from the transformation of the HG beams by a single lens AMC. The phase structures in the propagation evolution are also numerically manifested. We first demonstrate the transformation of the $\psi^{(\mathrm{HG})}_{N,0}(x, y, z)$ beam by a single lens AMC.

Figure 10 shows experimental results (first column) and theoretical calculations (second column) for the propagation evolution of the converted beam $\Psi_{9,0}(x, y, z; \zeta)$ with $\zeta = \pi/4$. Theoretical calculations can be found to agree excellently with experimental results for all propagating positions. The third column in Fig. 10 shows numerical results for the phase structures calculated by $\Theta_{n,m}(x, y, z; \zeta) = \arctan\,[\mathrm{Im}(\Psi_{n,m})/\mathrm{Re}(\Psi_{n,m})]$, where the relative range is given by the unit $\omega_o/\sqrt{2}$. It can be found that the phase structure outside the central part at $z = 0$ displays the hyperbolic feature. This characteristic is due to the fact that the phase factor $\Omega(\tilde{x}', \tilde{y}', z)$ in Eq. (56) for $z = 0$ is the hyperbolic form $-(\tilde{x}'^2 - \tilde{y}'^2)/2$. On the other hand, the phase factor $\Omega(\tilde{x}', \tilde{y}', z)$ for $z \to \infty$ is the circular expression $z(\tilde{x}'^2 + \tilde{y}'^2)/2z_R$. Consequently, the phase structures outside the central part change from the hyperbolic feature at $z = 0$ to the elliptical shape in the propagation and finally to the circular form in the far field for $z \to \infty$, as seen in the third column in Fig. 10. Near the central part, numerous isolated singularities appear in the phase structure for $0 < z < z_R$. There are $N = 9$

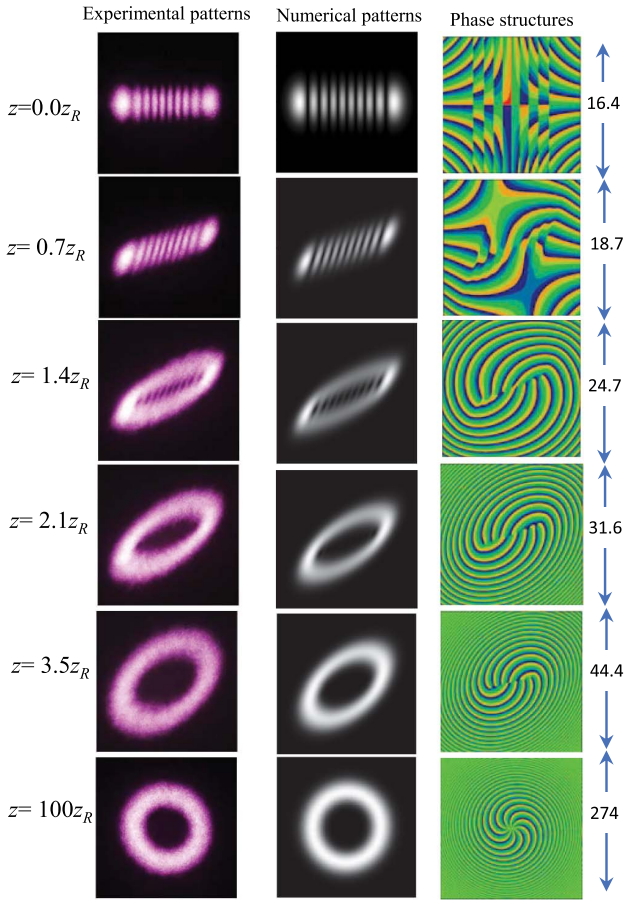

Fig. 10. Experimental results (first column), numerical wave patterns (second column), and phase structures (third column) for the propagation evolution of the converted beam $\Psi_{9,0}(x, y, z; \zeta)$ with $\zeta = \pi/4$. The number in the right side denotes the size of the pattern with the unit $\omega_o/\sqrt{2}$.

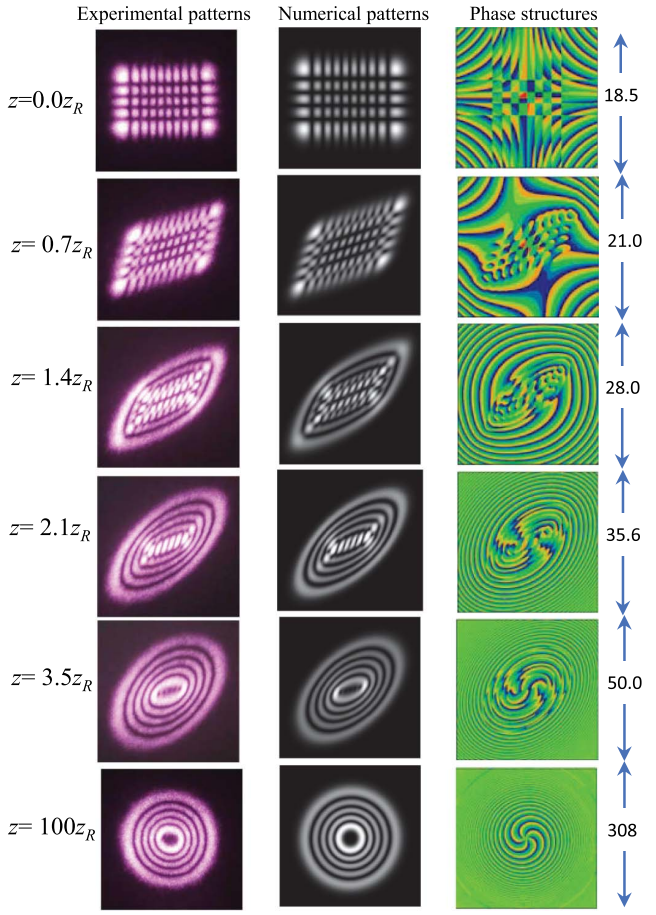

Fig. 11. Experimental results (first column), numerical wave patterns (second column), and phase structures (third column) for the propagation evolution of the converted beam $\Psi_{9,4}(x, y, z; \zeta)$ with $\zeta = \pi/4$. The number in the right side denotes the size of the pattern with the unit $\omega_o/\sqrt{2}$.

singularities with the topological charge one to be located as a linear array for $z > z_R$, as seen in the third column of Fig. 10. In the far field, the N singularities are merged into a single vortex with topological charge N, as the LG doughnut beam shown in the last row of Fig. 10.

Next, we discuss the case of the beam transformation for the $\psi^{(\mathrm{HG})}_{n,m}(x, y, z)$ mode with $n > m > 0$. Figure 11 shows experimental results (first column) and theoretical calculations (second column) for the propagation evolution of the converted beam $\Psi_{9,4}(x, y, z; \zeta)$ with $\zeta = \pi/4$. Theoretical calculations are also found to agree very well with experimental results for all propagating positions. Like the case in Fig. 10, the phase structures outside the central part change from the hyperbolic feature at $z = 0$ to the elliptical shape at $z > 0$ and finally to the circular form in the far field, as shown in the third column in Fig. 11. The phase structure near the central part can be seen to display a 2D array of isolated singularities for a short propagation distance $z < z_R$. In the far field, the 2D singularity array finally evolves into a single vortex with topological charge $n - m = 5$, as shown in the last row of Fig. 11.

The following is to demonstrate the beam transformation for the square HG modes $\psi^{(\mathrm{HG})}_{m,m}(x, y, z)$. Figure 12 shows experimental results (first column) and theoretical calculations (second column) for the propagation evolution of the converted beam $\Psi_{8,8}(x, y, z; \zeta)$ with $\zeta = \pi/4$. Once again, theoretical calculations are in excellent agreement with experimental results for all propagating positions. The phase structures outside the central part are generally similar to the discussed cases for a short propagation distance $z < z_R$, and the phase structure near the central part displays a 2D array of isolated singularities that are distributed in a rhombus shape, as seen in the third column of Fig. 12 for the result of $z = 0.7z_R$. Due to the square symmetry for the HG $\psi^{(\mathrm{HG})}_{m,m}(x, y, z)$ modes, all singularities annihilate, and no net vortices can exist in the far field, as shown in the last row of Fig. 12.

We finally present the beam transformation for the $\psi^{(\mathrm{HG})}_{n,m}(x, y, z)$ modes with $\zeta \neq \pi/4$. Figure 13 shows experimental results (first column) and theoretical calculations (second column) for the propagation evolution of the converted beam $\Psi_{9,4}(x, y, z; \zeta)$ with $\zeta = -5\pi/36$. Once again, theoretical calculations are in excellent agreement with

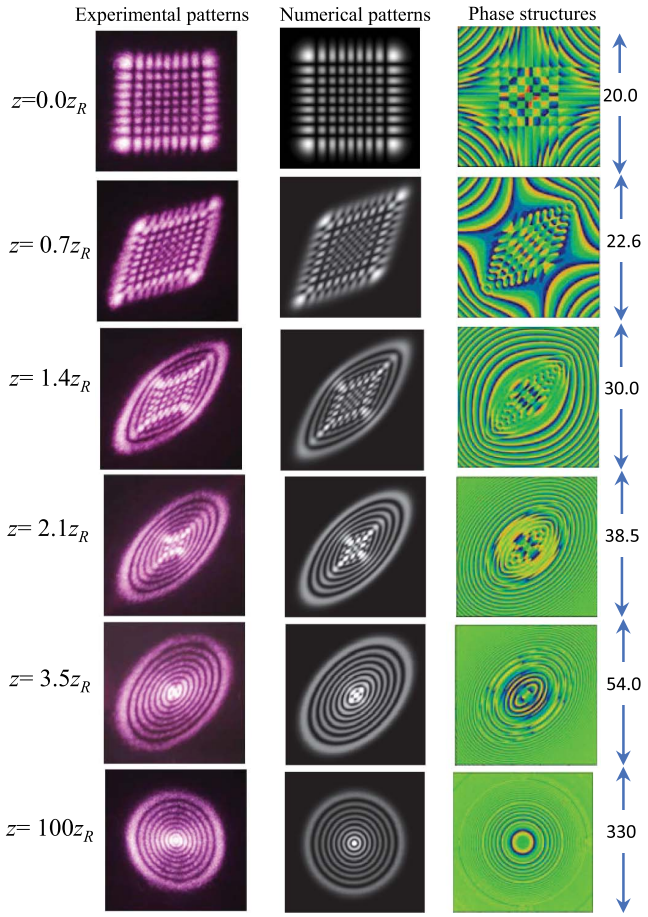

Fig. 12. Experimental results (first column), numerical wave patterns (second column), and phase structures (third coulmn) for the propagation evolution of the converted beam $\Psi_{8,8}(x, y, z; \zeta)$ with $\zeta = \pi/4$. The number in the right side denotes the size of the pattern with the unit $\omega_o/\sqrt{2}$.

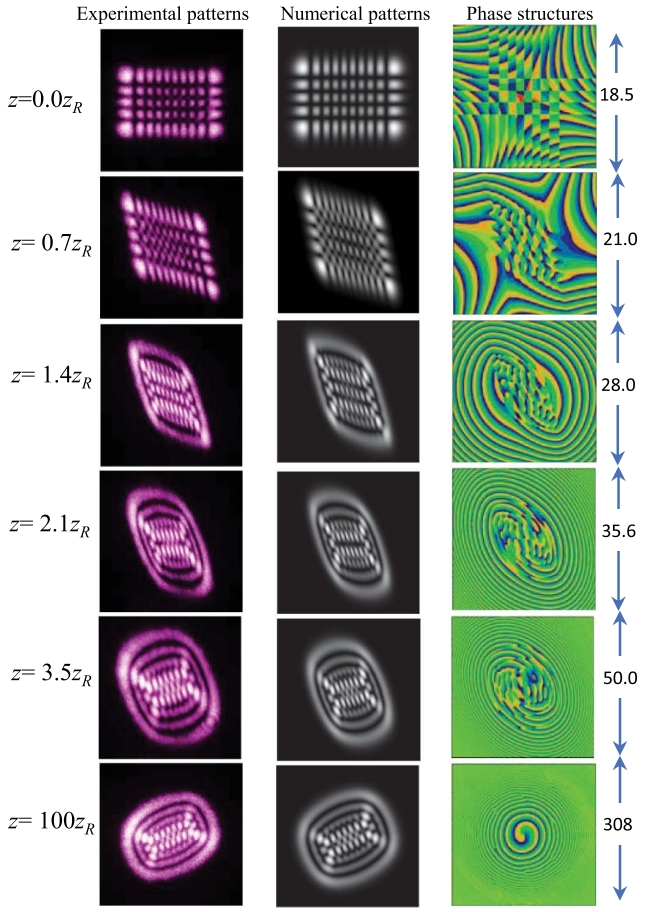

Fig. 13 Experimental results (first column), numerical wave patterns (second column), and phase structures (third column) for the propagation evolution of the converted beam $\Psi_{9,4}(x, y, z; \zeta)$ with $\zeta = -5\pi/36$. The number in the right side denotes the size of the pattern with the unit $\omega_o/\sqrt{2}$.

experimental observations for all propagating positions. The overall evolution of the phase structure in the propagation is like the case of $\zeta = \pi/4$ to display the vortex array just behind the AMC. The phase structure near the central part displays a 2D array of isolated singularities for a short propagation distance $z < z_R$. As shown in the last row of Fig. 13, the 2D singularity array in the far field finally evolves into a central vortex with charge one. There are also several vortices to be distributed around the central vortex. Due to $\zeta \neq \pi/4$, the topological charge of the central vortex is different from the case with $\zeta = \pi/4$, in which the topological charge is given by $n - m = 5$. Further research about the vortex distribution can be found in a previous paper[95].

In conclusion, we have thoroughly overviewed the theoretical description of the HLG modes from the representation of SU(2) in the Jordan–Schwinger map. Furthermore, we have discussed the derivation of representing the elliptical modes as an integration of the Gaussian wave-packet state over the elliptical trajectory. We have also overviewed the relationship between the HLG modes and elliptical modes based on the quantum Fourier transform. Finally, we have exploited the wave representation of the HLG modes to characterize the propagation evolution of the vortex structures of HG beams transformed by a single lens AMC. It is believed that the present review can provide not only a complete representation for transverse modes, but also a pedagogical insight into quantum physics.

This work was supported by the Ministry of Science and Technology of Taiwan (Contract No. 108-2119-M-009-005).

References

1. S. Flügge, *Practical Quantum Mechanics* (Springer-Verlag, 1971), p. 107.
2. H. Kogelnik and T. Li, Proc. IEEE **54**, 1312 (1966).
3. H. A. Haus, *Waves and Fields in Optoelectronics* (Prentice-Hall, 1984).
4. A. E. Siegman, *Lasers* (University Science Books, 1986)
5. Y. F. Chen, T. M. Huang, C. F. Kao, C. L. Wang, and S. C. Wang, IEEE J. Quantum Electron. **33**, 1025 (1997).
6. H. Laabs and B. Ozygus, Opt. Laser Technol. **28**, 213 (1996).
7. Y. F. Chen, C. C. Chang, C. Y. Lee, C. L. Sung, J. C. Tung, K. W. Su, H. C. Liang, W. D. Chen, and G. Zhang, Photon. Res. **5**, 561 (2017).

8. Y. F. Chen, C. C. Chang, C. Y. Lee, J. C. Tung, H. C. Liang, and K. F. Huang, Laser Phys. **28**, 015002 (2018).
9. Y. F. Chen and Y. P. Lan, Phys. Rev. A **63**, 063807 (2001).
10. C. J. Flood, G. Giuliani, and H. M. van Driel, Opt. Lett. **15**, 215 (1990).
11. J. F. Bisson, Y. Senatsky, and K. Ueda, Laser Phys. Lett. **2**, 327 (2005).
12. J. W. Kim and W. A. Clarkson, Opt. Commun. **296**, 109 (2013).
13. A. J. Lee, T. Omatsu, and H. M. Pask, Opt. Express **21**, 12401 (2013).
14. S. Ngcobo, K. Aït-Ameur, N. Passilly, A. Hasnaoui, and A. Forbes, Appl. Opt. **52**, 2093 (2013).
15. A. Hu, J. Lei, P. Chen, Y. Wang, and S. Li, Appl. Opt. **53**, 7845 (2014).
16. M. A. Bandres and J. C. Gutiérrez-Vega, J. Opt. Soc. Am. A **21**, 873 (2004).
17. U. T. Schwarz, M. A. Bandres, and J. C. Gutiérrez-Vega, Opt. Lett. **29**, 1870 (2004).
18. T. Ohtomo, K. Kamikariya, K. Otsuka, and S. Chu, Opt. Express **15**, 10705 (2007).
19. N. Barré, M. Romanelli, and M. Brunel, Opt. Lett. **39**, 1022 (2014).
20. K. Staliunas and V. J. Sanchez-Morcillo, *Transverse Patterns in Nonlinear Optical Resonators* (Springer, 2003).
21. M. Brambilla, F. Battipede, L. A. Lugiato, V. Penna, F. Prati, C. Tamm, and C. O. Weiss, Phys. Rev. A **43**, 5090 (1991).
22. D. Dangoisse, D. Hennequin, C. Lepers, E. Louvergneaux, and P. Glorieux, Phys. Rev. A **46**, 5955 (1992).
23. E. Louvergneaux, D. Hennequin, D. Dangoisse, and P. Glorieux, Phys. Rev. A **53**, 4435 (1996).
24. K. Staliunas, G. Slekys, and C. O. Weiss, Phys. Rev. Lett. **79**, 2658 (1997).
25. V. B. Taranenko, K. Staliunas, and C. O. Weiss, Phys. Rev. Lett. **81**, 2236 (1998).
26. E. Schrödinger, *Collected Papers on Wave Mechanics* (Chelsea, 1982).
27. P. Holland, *The Quantum Theory of Motion* (Cambridge University, 1993).
28. K. F. Huang, Y. F. Chen, H. C. Lai, and Y. P. Lan, Phys. Rev. Lett. **89**, 224102 (2002).
29. Y. F. Chen, Y. P. Lan, and K. F. Huang, Phys. Rev. A **68**, 043803 (2003).
30. Y. F. Chen, K. F. Huang, H. C. Lai, and Y. P. Lan, Phys. Rev. Lett. **90**, 052904 (2003).
31. Y. F. Chen, K. F. Huang, H. C. Lai, and Y. P. Lan, Phys. Rev. E **68**, 026210 (2003).
32. Y. F. Chen and Y. P. Lan, Phys. Rev. Lett. **93**, 013901 (2004).
33. Y. F. Chen, T. H. Lu, and K. F. Huang, Phys. Rev. Lett. **96**, 033901 (2006).
34. Y. F. Chen, T. H. Lu, K. W. Su, and K. F. Huang, Phys. Rev. Lett. **96**, 213902 (2006).
35. Y. F. Chen, K. W. Su, T. H. Lu, and K. F. Huang, Phys. Rev. Lett. **96**, 033905 (2006).
36. Y. F. Chen, T. H. Lu, and K. F. Huang, Phys. Rev. Lett. **97**, 233903 (2006).
37. T. H. Lu, Y. C. Lin, Y. F. Chen, and K. F. Huang, Phys. Rev. Lett. **101**, 233901 (2008).
38. C. C. Chen, Y. T. Yu, Ross C. C. Chen, Y. J. Huang, K. W. Su, Y. F. Chen, and K. F. Huang, Phys. Rev. Lett. **102**, 044101 (2009).
39. J. Courtois, A. Mohamed, and D. Romanini, Phys. Rev. A **88**, 043844 (2013).
40. Y. T. Yu, P. H. Tuan, P. Y. Chiang, H. C. Liang, K. F. Huang, and Y. F. Chen, Phys. Rev. E **84**, 056201 (2011).
41. J. C. Tung, P. H. Tuan, H. C. Liang, K. F. Huang, and Y. F. Chen, Phys. Rev. A **94**, 023811 (2016).
42. J. Durnin, J. J. Miceli, and J. H. Eberly, Phys. Rev. Lett. **58**, 1499 (1987).
43. M. W. Beijersbergen, R. P. C. Coerwinkel, M. Kristensen, and J. P. Woerdman, Opt. Commun. **112**, 321 (1994).
44. G. A. Siviloglou, J. Broky, A. Dogariu, and D. N. Christodoulides, Phys. Rev. Lett. **99**, 213901 (2007).
45. A. Yu Okulov and A. N. Oraevsky, J. Opt. Soc. Am. B **3**, 741 (1986).
46. Y. F. Chen and Y. P. Lan, Phys. Rev. A **65**, 013802 (2001).
47. A. Yu Okulov, Laser Phys. **19**, 1796 (2009).
48. V. L. Berezinskii, Sov. Phys. JETP **34**, 610 (1972).
49. J. M. Kosterlitz and D. J. Thouless, J. Phys. C: Solid State Phys. **6**, 1181 (1973).
50. Z. Hadzibabic, P. Krüger, M. Cheneau, B. Battelier, and J. Dalibard, Nature **441**, 1118 (2006).
51. A. Yu Okulov, Phys. Rev. A **80**, 013837 (2009).
52. J. F. Nye and M. V. Berry, Proc. R. Soc. London **336**, 165 (1974).
53. M. S. Soskin and M. V. Vasnetsov, Prog. Opt. **42**, 219 (2001).
54. L. Allen, M. W. Beijersbergen, R. J. C. Spreeuw, and J. P. Woerdman, Phys. Rev. A **45**, 8185 (1992).
55. G. Indebetouw, J. Mod. Opt. **40**, 73 (1993).
56. D. L. Andrews, *Structured Light and Its Applications: An Introduction to Phase-structured Beams and Nanoscale Optical Force* (Academic, 2008).
57. E. Santamato, A. Sasso, B. Piccirillo, and A. Vella, Opt. Express **10**, 871 (2002).
58. K. T. Gahagan and G. A. Swartzlander, Jr., Opt. Lett. **21**, 827 (1996).
59. L. Paterson, M. P. MacDonald, J. Arlt, W. Sibbett, P. E. Bryant, and K. Dholakia, Science **292**, 912 (2001).
60. M. P. MacDonald, Opt. Commun. **201**, 21 (2002).
61. Y. Song, D. Milam, and W. T. Hill, Opt. Lett. **24**, 1805 (1999).
62. X. Xu, K. Kim, W. Jhe, and N. Kwon, Phy. Rev. A **63**, 3401 (2001).
63. T. Kuga, Y. Torii, N. Shiokawa, T. Hirano, Y. Shimizu, and H. Sasada, Phys. Rev. Lett. **78**, 4713 (1997).
64. J. Courtial, D. A. Robertson, K. Dholakia, L. Allen, and M. J. Padgett, Phys. Rev. Lett. **81**, 4828 (1998).
65. J. Courtial, K. Dholakia, D. A. Robertson, L. Allen, and M. J. Padgett, Phys. Rev. Lett. **80**, 3217 (1998).
66. A. Mair, A. Vaziri, G. Weihs, and A. Zeilinger, Nature **412**, 313 (2001).
67. N. R. Heckenberg, R. McDuff, C. P. Smith, and A. G. White, Opt. Lett. **17**, 221 (1992).
68. M. W. Beijersbergen, L. Allen, H. E. L. O. van der Veen, and J. P. Woerdman, Opt. Commun. **96**, 123 (1993).
69. E. G. Abramochkin and V. G. Volostnikov, Opt. Commun. **83**, 123 (1991).
70. J. Pollet, O. Méplan, and C. Gignoux, J. Phys. A **28**, 7282 (1995).
71. I. V. Zozoulenko and K. F. Berggren, Phys. Rev. B **56**, 6931 (1997).
72. R. Brunner, R. Meisels, F. Kuchar, R. Akis, D. K. Ferry, and J. P. Bird, Phys. Rev. Lett. **98**, 204101 (2007).
73. A. D. Peters, C. Jaffé, and J. B. Delos, Phys. Rev. Lett. **73**, 2825 (1994).
74. C. Bracher and J. B. Delos, Phys. Rev. Lett. **96**, 100404 (2006).
75. M. Brack, Rev. Mod. Phys. **65**, 677 (1993).
76. W. A. De Heer, Rev. Mod. Phys. **65**, 611 (1993).
77. Y. F. Chen and Y. P. Lan, Phys. Rev. A **66**, 053812 (2002).
78. Y. F. Chen and Y. P. Lan, Phys. Rev. A **67**, 043814 (2003).
79. J. Banerji and G. S. Agarwal, Opt. Express **5**, 220 (1999).

80. Y. F. Chen, Y. H. Hsieh, and K. F. Huang, OSA Continuum **1**, 744 (2018).
81. J. Schwinger, *Quantum Theory of Angular Momentum*, L. C. Biedenharn and H. van Dam, eds. (Academic, 1965), p. 229.
82. V. V. Kotlyar, A. A. Kovalev, and A. P. Porfirev, Opt. Lett. **42**, 139 (2017).
83. V. V. Kotlyar, A. A. Kovalev, and A. P. Porfirev, Opt. Lett. **40**, 701 (2015).
84. E. G. Abramochkin and V. G. Volostnikov, J. Opt. A: Pure Appl. Opt. **6**, S157 (2004).
85. W. N. Plick, M. Krenn, R. Fickler, S. Ramelow, and A. Zeilinger, Phys. Rev. A **87**, 033806 (2013).
86. V. V. Kotlyar, A. A. Kovalev, and A. P. Porfirev, Phys. Rev. A **87**, 033806 (2013).
87. Y. F. Chen, Phys. Rev. A **83**, 032124 (2011).
88. P. Jordan, Zeitschrift für Physik **94**, 531 (1935).
89. J. J. Sakurai and J. J. Napolitano, *Modern Quantum Mechanics* (Pearson, 2010).
90. E. P. Wigner, *Gruppentheorie und ihre Anwendungen auf die Quantenmechanik der Atomspektren* (Vieweg Verlag, 1931). Translated into English by J. J. Griffin, *Group Theory and Its Application to the Quantum Mechanics of Atomic Spectra* (Academic Press, 1959).
91. N. N. Lebedev, *Special Functions & Their Applications* (Dover, 1972).
92. R. Blüumel, *Foundations of Quantum Mechanics: From Photons to Quantum Computers* (Jones and Bartlett, 2010).
93. H. Sridhar, M. G. Cohen, and J. W. Noé, Proc. SPIE **7613**, 76130X (2010).
94. H. A. Nam, M. G. Cohen, and J. W. Noé, J. Opt. **13**, 064026 (2011).
95. Y. H. Hsieh, Y. H. Lai, M. X. Hsieh, and Y. F. Chen, Opt. Lett. **45**, 200 (2020).